Crystallization of Ge2Sb2Te5 films by amplified femtosecond optical pulses

Y. Liu, M. M. Aziz, A. Shalini, C. D. Wright, and R. J. Hicken

Additional information on J. Appl. Phys.

Crystallization of Ge$_2$Sb$_2$Te$_5$ films by amplified femtosecond optical pulses

Y. Liu,[1] M. M. Aziz,[2] A. Shalini,[1] C. D. Wright,[2] and R. J. Hicken[1]
[1]*School of Physics and Astronomy, University of Exeter, Stocker Road, Exeter EX4 4QL, United Kingdom*
[2]*College of Engineering, Mathematics and Physical Sciences, University of Exeter, North Park Road, Exeter, EX4 4QF, United Kingdom*

The phase transition between the amorphous and crystalline states of Ge$_2$Sb$_2$Te$_5$ has been studied by exposure of thin films to series of 60 femtosecond (fs) amplified laser pulses. The analysis of microscope images of marks of tens of microns in size provide an opportunity to examine the effect of a continuous range of optical fluence. For a fixed number of pulses, the dependence of the area of the crystalline mark upon the fluence is well described by simple algebraic results that provide strong evidence that thermal transport within the sample is one-dimensional (vertical). The crystalline mark area was thus defined by the incident fs laser beam profile rather than by lateral heat diffusion, with a sharp transition between the crystalline and amorphous materials as confirmed from line scans of the microscope images. A simplified, one-dimensional model that accounts for optical absorption, thermal transport and thermally activated crystallization provides values of the optical reflectivity and mark area that are in very good quantitative agreement with the experimental data, further justifying the one-dimensional heat flow assumption. Typically, for fluences below the damage threshold, the crystalline mark has annular shape, with the fluence at the centre of the irradiated mark being sufficient to induce melting. The fluence at the centre of the mark was correlated with the melt depth from the thermal model to correctly predict the observed melt fluence thresholds and to explain the closure and persistence of the annular crystalline marks as functions of laser fluence and pulse number. A solid elliptical mark may be obtained for smaller fluences. The analysis of marks made by amplified fs pulses present a new and effective means of observing the crystallization dynamics of phase-change material at elevated temperatures near the melting point, which provided estimates of the growth velocity in the range 7-9 m/s. Furthermore, finer control over the crystallization process in phase-change media can be obtained by controlling the number of pulses which, along with the laser fluence, can be tailored to any medium stack with relaxed restrictions on the thermal properties of the layers in the stack. © *2012 American Institute of Physics*. [http://dx.doi.org/10.1063/1.4770359]

I. INTRODUCTION

Chalcogenide alloys, such as Ge$_2$Sb$_2$Te$_5$ (GST) possess a unique combination of structural, electrical, and optical properties.[1] The amorphous and crystalline states of these materials exhibit a very large difference in optical reflectivity and electrical resistance, while the transition between the two phases may be achieved reversibly on very short time-scales by applying optical or electrical pulses. Despite their widespread application as optical phase-change recording media and great effort being made to establish the optimum conditions for the phase transition,[2–10] inconsistencies remain within the literature. For example, there is disagreement about the minimum pulse duration and optimum pump fluence required to induce the phase transition, and about whether crystallization can be induced by application of a single femtosecond optical pulse.

In this paper, we investigate the phase transition induced in GST films by multiple femtosecond optical pulses from a regenerative laser amplifier system. By continuously varying the laser fluence, we also investigate crystallization directly from the amorphous phase and from the molten phase. While sub-micron spot sizes are used within optical disk drive technology to maximize data storage capacity, the use of fs pulses

of μJ energy allows experiments to be performed with focused spots that are some tens of microns in diameter that provide a wealth of information about the crystallization process. From the form of the marks, we show that thermal transport within the sample is one-dimensional for large area fs excitation through simple geometrical models relating the crystalline mark area to the laser beam profile. Since the intensity profile of the fs laser spot has been carefully measured, the images reveal the dependence of the crystallization upon a continuous range of laser fluence and pulse number. It is also shown that a mark can be re-amorphized by a single fs pulse of sufficient fluence. Simple analytical models of heat conduction and reaction rate are developed to study the thermally activated crystallization process under femtosecond laser excitation. The models confirmed the one-dimensional nature of heat flow towards the substrate under fs laser excitation with the calculated values of the reflectivity and crystalline mark areas following closely the experimental measurements. The theoretical models are also used to explain the formation, closure and persistence of crystalline annular rings and their dependence on laser fluence and pulse number. Finally, with successive fs laser pulses, the closure of the annular crystalline rings was captured at discrete times with the optical microscope to estimate crystal growth rates at elevated temperatures.

II. EXPERIMENTAL DETAILS

Amorphous GST films of 20 nm thickness were sputter deposited at room temperature onto Si(001) substrates coated with a ZnS:SiO$_2$ underlayer of 310 nm thickness. The ZnS:SiO$_2$ dielectric layer provides a means of controlling the thermal contact with the underlying substrate. The films were capped with a 30 nm layer of ZnS:SiO$_2$ to provide protection against oxidation. The precise values of the layer thicknesses within the stack are also adjusted to maximize the reflectivity contrast between the crystalline and amorphous states.[1]

Optical measurements were performed within a "pump-probe" type configuration with the pump and probe beams focused onto the sample surface within the focal plane of an optical microscope equipped with a 20× objective lens and an intensity calibrated Leica DFC295 CCD camera. A Coherent Ti-Sapphire regenerative amplifier (RegA) system was used to generate pump pulses of 800 nm wavelength, 60 fs duration (determined from intensity autocorrelation width measurement of 85 fs with a Gaussian time profile), energy of up to 8 μJ, and repetition rate from 300 kHz to single shot. A continuous wave He-Ne laser of 633 nm wavelength was used as a probe that could provide a continuous record of the sample reflectivity during excitation. Series of microscope images were acquired using a white light source and a 632/25 nm bandpass filter so that reflectivity changes measured with the microscope and with the probe beam could be directly compared. A DataRay WinCamD-UCD12 beam profiler with 4.65 μm pixel size was first inserted in place of the sample and used to obtain optimum overlap of the two focused spots within the focal plane of the microscope. The profiler confirmed that the intensity profiles of the spots along their principal axes were Gaussian and was used to determine the spot size defined by the $1/e^2$ intensity level. The s-polarized pump beam was incident at an angle of 43° and was focused to an 85 μm × 65 μm elliptical spot, while the s-polarized probe beam had angle of incidence of 51° and spot size of 69 μm × 46 μm. The spot size is defined by the distance between the $1/e^2$ points along the principal axes of the spot. A computer-controlled arbitrary waveform generator was used to trigger the regenerative amplifier and hence generate series of pump pulses of variable number and repetition rate. Contour and line profiles of the reflectivity of the written mark were obtained from the acquired microscope images.

III. EXPERIMENTAL RESULTS

Single fs pulses were first used to excite the GST film. The effect of excitation by pulses of different fluence is shown in Fig. 1. It is clearly seen that a single pulse with 60 fs duration cannot crystallize the film. Defining the average fluence F_{avg} as the pulse energy divided by the $1/e^2$ area of the spot, there is either no visible effect for F_{avg} values smaller than 17.5 mJ/cm^2 or else permanent damage occurs for larger F_{avg} values, with the damaged area increasing with F_{avg}.

Although a single pulse with small F_{avg} may not produce any visible effect, it may modify the size distribution of
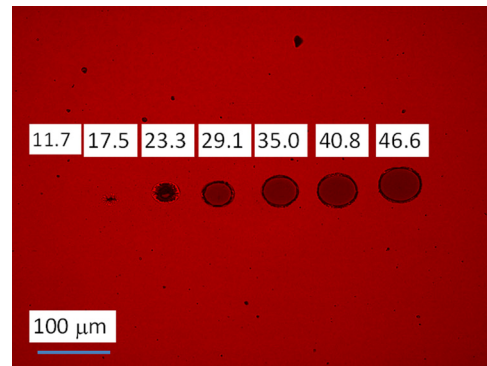

FIG. 1. Optical microscope image of the marks obtained after excitation by single pulses of 60 fs duration. The value of the spatially averaged pulse fluence F_{avg} (mJ/cm^2) is shown.

nanometer scale crystalline nuclei that grow and coalesce during the crystallization process.[11] In order to explore this process further, the sample was next exposed to multiple fs pulses. Images acquired after exposure to 2000 pulses of different F_{avg} values are shown in Fig. 2. Four different regions may be identified: (i) for F_{avg} less than 2.57 mJ/cm^2, no change in reflectivity is observed; (ii) for F_{avg} between 2.57 and 4.43 mJ/cm^2, homogeneous elliptical marks are observed, the reflectivity within the area of the mark being higher than that of the amorphous background; (iii) for F_{avg} between 4.66 and 9.33 mJ/cm^2, elliptical annuli are formed, in which the central region enclosed by the annulus has similar reflectivity to the amorphous state; (iv) for F_{avg} greater than 10.5 mJ/cm^2, annuli are again observed, but the reflectivity at the center of the enclosed region is smaller than that of the amorphous film indicating irreversible damage.

Line profiles of reflectivity taken along the major axis of selected marks are shown in Fig. 3. Examples from region (ii), $F_{avg} = 3.50$ mJ/cm^2, and region (iii), $F_{avg} = 5.83$ mJ/cm^2, are shown in Figs. 3(a) and 3(b), respectively. In Fig. 3(a), the reflectivity shows a sharp increase at the outer perimeter of the mark, indicating a phase boundary between the crystalline interior and the surrounding amorphous film. The reflectivity is slightly lower at the centre of the mark relative to the rest of the crystallized region. In Fig. 3(b), the cross section through an annulus reveals that the reflectivity within the central enclosed region is the same as that of the
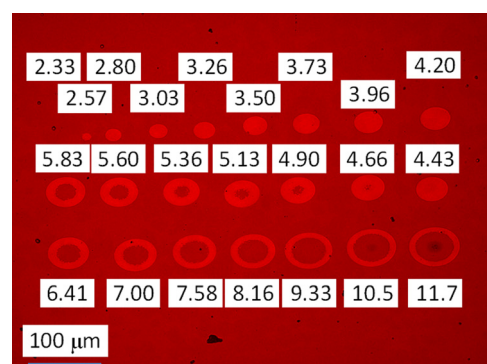

FIG. 2. Optical microscope images of the marks obtained after excitation by a series of 2000 pulses of 60 fs duration. The value of the spatially averaged pulse fluence F_{avg} (mJ/cm^2) is shown.
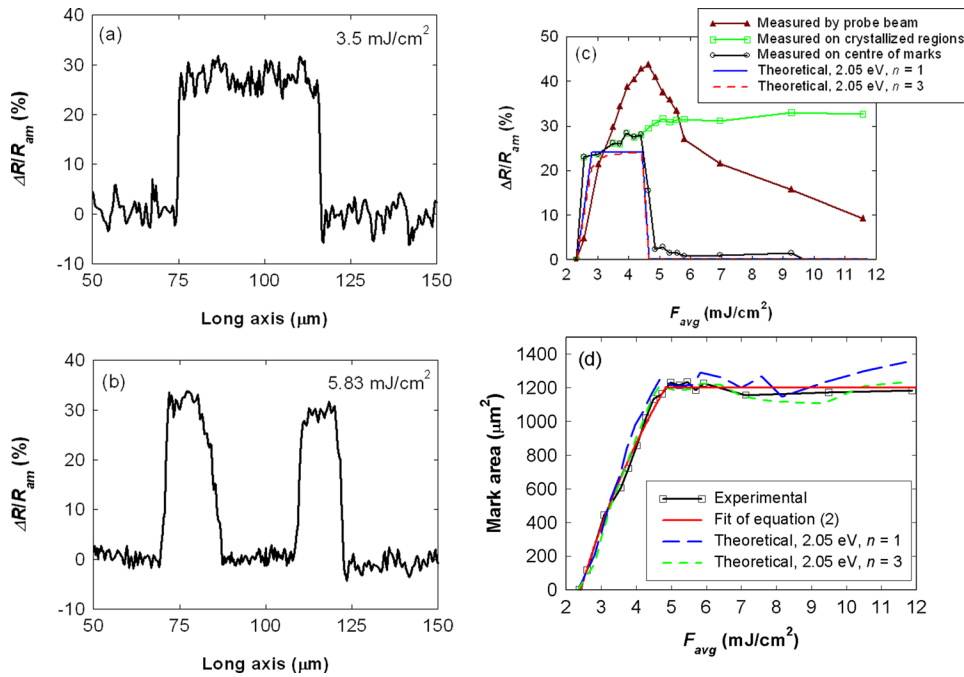
FIG. 3. The change in reflectance of $Ge_2Sb_2Te_5$ films $\Delta R/R_{am}$ (defined as $\Delta R = R - R_{am}$ where R is the measured reflectance and R_{am} is the reflectance of the as-deposited amorphous material) after exposure to 2000 pulses of 60 fs pulse width is shown for different values of F_{avg} (the spatially averaged fluence). Spatial profiles of marks recorded for F_{avg} values of 3.50 and 5.83 mJ/cm² are shown in panels (a) and (b) respectively. Panel (c) shows the measured variation of the maximum reflectance within the area of the mark (squares), the reflectance at the centre of the mark (circles), and relative change of reflectivity measured by the probe beam (triangles) compared with the theoretical reflectance change at the centre of the mark (solid and dashed lines). The dependence of the area of the high reflectance region upon F_{avg} is shown in (d), where the black squares are experimental data, the red solid curve is from the geometrical fit and the dashed lines are calculated from the crystallization model.

amorphous film. This implies that the local fluence at the centre of the mark is sufficiently large that the GST melts before being rapidly quenched to the amorphous state. The reflectivity towards the outer perimeter of the annulus is slightly larger than that within the solid mark of Fig. 3(a), and the reflectivity is seen to decrease somewhat towards the inner perimeter. The transition between high and low reflectivity is generally less sharp at the inner perimeter compared to that at the outer perimeter. In Fig. 3(c), the relative changes in reflectivity determined from the microscope images and by the probe beam are plotted for comparison. The black circles represent the reflectivity values at the center of the mark while the green squares represent the reflectivity half way between the inner and outer perimeters of the annulus once it has formed. The microscope images reveal a large change in reflectivity of about 23% as the film first crystallizes. When F_{avg} reaches a value of 4.43 mJ/cm², the reflectivity at the center of the mark decreases to amorphous state level as the annulus is first formed. The reflectivity change at the half way position within the annulus gradually increases with F_{avg}, as the crystalline fraction increases, before saturating at a value of about 32% when F_{avg} exceeds 5.13 mJ/cm². This increased reflectance at the outer perimeter of the crystalline marks most likely indicates the formation of the hexagonal crystalline phase in this region and will be analysed later in the discussion. The laser probe beam was also used to record the change of reflectivity. Since the spot size of the probe beam is larger than the size of the crystallized marks, the recorded reflectivity change depends upon both the change in reflectivity between the amorphous and crystalline states, and also the area and location of the crystallized region. The change in reflectance detected by the laser probe beam increases as the pulse fluence increases until the annulus is formed, but then decreases with further increase of fluence as the region of high reflectance within the annulus moves outwards from the region of maximum

probe beam intensity. The maximum value of the relative change of reflectivity obtained with the laser probe beam is significantly larger than that obtained from the microscope images. This is due to the different angles of incidence of the probe beam and microscope illumination (51° and normal incidence, respectively). Figure 3(d) shows that the area of the high reflectivity region increases monotonically with F_{avg} until $F_{avg} = 4.43$ mJ/cm², after which it remains approximately constant. This implies that for large F_{avg} values the width of the annulus decreases as its outer perimeter increases so as to leave its area constant. The area of the region of high reflectivity was defined as being that in which the reflectivity lay above the median value.

Clearly the total fluence delivered to the film may be controlled via either the fluence of an individual pulse or the number of pulses used. Figure 4 shows the effect of using different number of pulses for different fluence values. The fluence of an individual pulse is fixed within each row of marks in Fig. 4(a). Moving to the right along each row and starting with 200 pulses, the number of pulses increases by 50 for each successive mark and is equal to 600 for the mark at the far right (with the exception of the labeled mark produced after 1150 pulses at the lowest fluence and included for comparison). For the range of fluences $F_{avg} = 3.26 - 4.43$ mJ/cm², the minimum number of optical pulses required for the appearance of a high reflectance mark is nearly the same between 200 and 250. We will return later to the complicated relationship between the spatial variation of the optically induced temperature transient and the shape of the mark. For now we note that crystallization first occurs where the optically induced temperature is optimal (somewhat below the melting temperature). For small F_{avg}, crystallization is first observed at the centre of the pump spot, but as F_{avg} is increased the temperature at the centre exceeds the melting temperature (as the heat flow calculations show) and so crystallization first occurs at a finite distance from the centre of
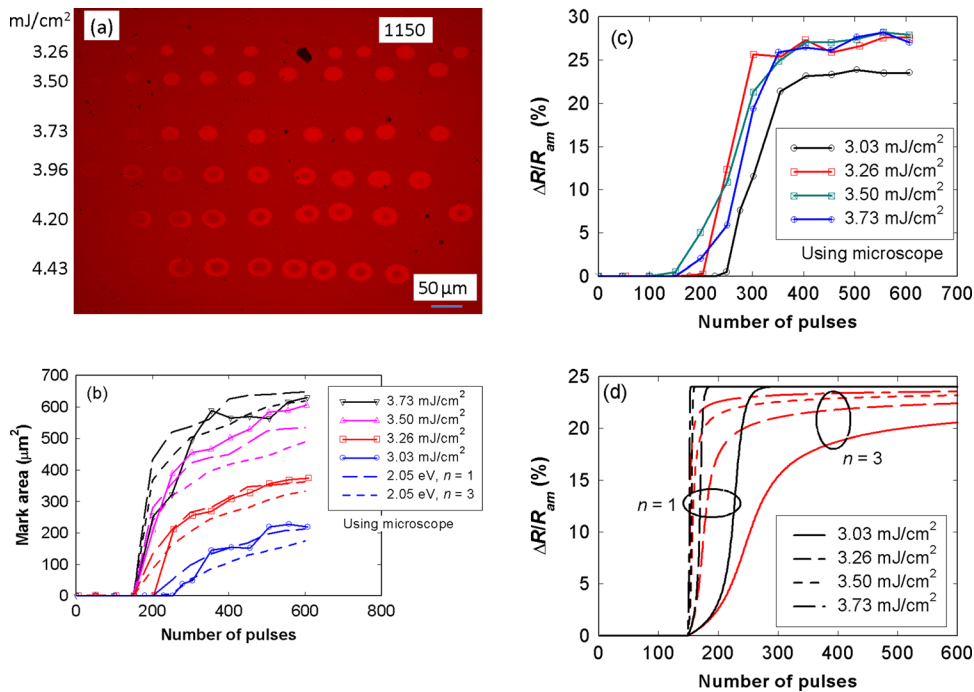
FIG. 4. The dependence of crystallisation upon the number of 60 fs pulses and F_{avg}. (a) microscope images of marks where the values of F_{avg} have been labelled and the number of pulses varies from 200 at the far left to 600 at the far right with increment of 50. In (b), (c) the dependence of the area of the crystallised region, and the relative change of reflectivity, at the high reflectivity crystalline region, respectively upon the number of pulses is shown for different F_{avg} values. The dashed lines in (b) are the calculated mark areas using the thermal and crystallization models. (d) Calculated optical reflectance curves as a function of pulse number corresponding to the experimental curves in (c) from the crystallization model for two reaction orders, $n = 1, 3$.

the spot where the temperature is below melting, leading to the formation of an annulus of higher reflectance at the periphery. Where an annulus is formed, the length of its outer perimeter increases and that of its inner perimeter decreases as the number of pulses is increased. The marks in Fig. 4(a) can be used to identify the value of the pump fluence for which the temperature at the center of mark exceeds the melting temperature. This is the fluence 3.73 mJ/cm^2 which clearly marks the appearance of the crystalline annulus. Figure 4(b) shows the dependence of the area of the high reflectivity region upon the number of pulses when F_{avg} is less than the value required for melting. For a given number of pulses the area is seen to depend strongly upon F_{avg} when F_{avg} is small before saturating for larger F_{avg} values. Figure 4(c) shows how the relative change of reflectivity within the high reflectance area of the mark depends upon the number of pulses. The minimum number of pulses needed for the onset of change in reflectivity decreases with increasing fluence due to the increased temperature in the GST layer which increases the nucleation rate and reduces the incubation time. The change of reflectivity is relatively insensitive to F_{avg} once the mark is formed. When the pulse fluence was further reduced below 3.26 mJ/cm^2 (not shown here) the minimum number of pulses required to induce a change of reflectance increased very significantly. About 1000 pulses were required to induce a noticeable increase in reflectivity for $F_{avg} = 2.57$ mJ/cm^2, while 2000 pulses were insufficient to modify the reflectivity when $F_{avg} = 2.33$ mJ/cm^2.

Further measurements were performed with pump pulses of different widths and repetition rates. The pulse width was varied continuously between 60 fs and 1.4 ps by adjusting the compressor stage of the regenerative amplifier and monitoring the pulse width with an autocorrelator, while the pulse repetition rate was adjusted from 4 to 300 kHz by controlling the rate of injection of seed pulses to the amplifier cavity. There was no noticeable dependence of the mark profile upon either the pulse width or the repetition rate. Crystallization and mark formation in this case are governed by heat diffusion which occurs over time scales much longer than the laser pulse widths and non-equilibrium processes (which occur within 5 ps for Ge$_2$Sb$_2$T$_5$).[12] Moreover, the slow repetition rates (compared to the nanosecond relaxation time of temperature after the application of a laser pulse) ensure negligible heat accumulation and storage between pulses to affect mark formation.

Erasable data storage applications require the phase transition between amorphous and crystalline states to be reversible. Therefore, further measurements with increased fluence were performed to explore the conditions for amorphization by femtosecond laser pulses. Figure 5(a) shows a mark made by 2000 pulses of 60 fs duration with $F_{avg} = 3.50$ mJ/cm^2. Figure 5(b) shows that the mark was completely reamorphized by a single pulse with $F_{avg} = 9.33$ mJ/cm^2. In fact single pulse amorphization could be achieved for F_{avg} values ranging from 7.6 mJ/cm^2 to 11.7 mJ/cm^2, with damage occurring for larger values of the fluence. Moreover, it was found that the phase transition between amorphous and crystalline states could be repeated. Five cycles of crystallization and amorphization were performed for the mark shown in Fig. 5 although we expect that many thousands of cycles should be possible before the material suffers irreversible fatigue. Scanning electron microscopy (SEM) and atomic force microscopy (AFM) imaging could be useful in providing further details on the laser induced changes in the GST film, and final state of the material after writing.

A. Mark area and laser fluence

While crystallization could not be achieved with a single fs pulse for the thin-film stack studied in the present work, excitation by multiple fs pulses led to the appearance of marks of higher reflectivity that indicate that crystallization
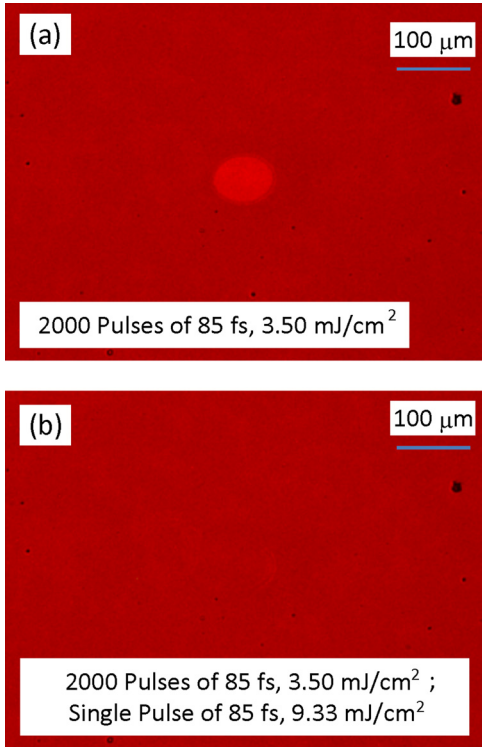
FIG. 5. (a) Microscope image of crystallised mark obtained using 2000 pulses of 60 fs duration with $F_{avg} = 3.50$ mJ/cm^2. (b) Microscope image after re-amorphization using a single 60 fs pulse with $F_{avg} = 9.33$ mJ/cm^2.

had taken place. The marks have features that depend sensitively upon the number and spatially averaged fluence F_{avg} of the pulses. Consider first the case that the number of pulses was kept constant as shown in Fig. 3(d). As F_{avg} was increased beyond a threshold value, the area of the mark increased rapidly, before saturating as the shape of the mark changed from a solid ellipse to an annulus of approximately constant area. Let the position dependent fluence within the focused pump spot have the form:

$$I(x,y) = I_0 \exp\left\{-\left[\left(\frac{x}{a}\right)^2 + \left(\frac{x}{b}\right)^2\right]\right\} \qquad (1)$$

where I_0 is the peak fluence, and a and b are the $1/e$ radii along the x and y semi-principal axes of the elliptically shaped spot. The locus of points of equal intensity may be labeled by the parameter u where $u^2 = (x/a)^2 + (y/b)^2$ and corresponds to an ellipse with semi-principal axes of lengths ua and ub and area $u^2\pi ab$. I_0 is related to the $1/e^2$ average fluence F_{avg} by considering the locus of points at which $I = I_0/e^2$ (where $u = \sqrt{2}$) to define an ellipse with semi-principal axes of lengths $\sqrt{2}a$ and $\sqrt{2}b$ and therefore area $2\pi ab$. F_{avg} is then derived from the total pulse energy (obtained by integrating (1) between $\pm$ infinity in the x and y directions) divided by the $1/e^2$ beam area ($2\pi ab$) to yield $F_{avg} = I_0/2$, therefore defining the peak fluence as $I_0 = 2F_{avg}$.

If the transport of heat within the sample is one-dimensional (with no lateral heat flow) then each value of u corresponds to a distinct intensity and value of the maximum temperature T_{max} reached during the excitation process. Let u_m correspond to the intensity I_m at which T_{max} is equal to

the melting temperature, and u_c correspond to an intensity I_c for which the value of T_{max} is just sufficient for crystallization for the 2000 pulses used in the experiment. The maximum intensity I_0 occurs at the centre of the pump spot and so for $I_0 < I_c$, there is no crystallization at any value of u, but for $I_c < I_0 < I_m$ an elliptical mark is obtained with area given by:

$$
\begin{aligned}
A &= \pi ab u_c^2 = \pi ab[\ln(I_0) - \ln(I_c)] \\
&= \pi ab[\ln(F_{avg}) + \ln(2/I_c)]. \qquad (2)
\end{aligned}
$$

Fitting this equation to the rising part of the experimental curve in Fig. 3(d) yields $\pi ab = 1730\ \mu m^2$ and $I_c = 4.77$ mJ/cm^2. Using the values of $a = 30\ \mu m$ and $b = 23\ \mu m$ measured with the beam profiler yields an area of $\pi ab = 2168\ \mu m^2$. This is 20% larger than that deduced from the fit to Fig. 3(d) but corresponds to only a 10% discrepancy in the determination of the linear dimensions of the ellipse.

Once an annular mark has formed, its area A may be written as:

$$
\begin{aligned}
A &= \pi ab[u_c^2 - u_m^2] = \pi ab[\ln(I_0/I_c) - \ln(I_0/I_m)] \\
&= \pi ab\ln(I_m/I_c), \qquad (3)
\end{aligned}
$$

which is independent of the pump intensity I_0, or equivalently F_{avg}, as indicated by the saturated part of the experimental curve in Fig. 3(d). Taking this area to be equal to $A \sim 1200$ μm^2 from Fig. 3(d) and using $I_c = 4.77$ mJ/cm^2 from the previous fitting, we deduce that the local threshold fluence required for melting is $I_m = 9.54$ mJ/cm^2 ($F_{avg} = 4.77$ mJ/cm^2) which is in very good agreement with the melt threshold predicted from modelling as will be later shown. Equations (2) and (3) provide a very good description of the data within Fig. 3(d), supporting the assumption that the thermal transport is essentially one dimensional (vertical), as might be expected given the large aspect ratio of the optically pumped region of the GST film. This was also observed in amorphization experiments where the size of the amorphous marks formed under femtosecond laser irradiation was defined primarily by the laser beam distribution, without a surrounding crystalline band edge due to the negligible heat diffusion at femtosecond and picosecond time scales.[7,13] Moreover at higher laser intensities, the generated hot carriers-phonon interaction in the surface of the GST material at these short time scales could enhance the scattering and reduce lateral carrier diffusion and lateral heat transport.[12]

IV. HEAT FLOW AND CRYSTALLIZATION MODELS

So far we have implicitly assumed that the onset of crystallization is sufficiently rapid that different regions of the sample may be described as being either amorphous or fully crystalline. However, the curves of Figs. 3(c) and 4(c) reveal that there are a range of values of the pump fluence and number of pulses where the value of the reflectivity varies continuously between those for the amorphous and fully crystallized states. To reproduce these variations, it is necessary to calculate the temperature profile T induced within the

film by each successive laser pulse by including the spatial and temporal variation of the optical power density within the heat diffusion equation. The values of a number of material parameters are expected to evolve with time as crystallization occurs and so it is necessary to simultaneously consider the crystallization kinetics. This in turn allows the optical constants to be deduced through the use of an effective medium theory, which can then be fed back into the heat diffusion equation so that the power absorbed from the next pulse can be recalculated as crystallization proceeds. The material parameters during a particular pulse are assumed constant, considering the very small change in crystalline fraction induced by an individual fs laser pulse. The simplified analytical models described below provide a method for rapidly calculating the temperature and crystalline volume fraction in the GST layer due to the application of hundreds and thousands of laser pulses, and for mitigating the numerical difficulties in solving this complex system quickly with relative accuracy at very short time scales and divergent length scales (tens of micrometers size laser spot versus nanometer thick layers).

Reported transient reflectivity measurements of amorphous $Ge_2Sb_2Te_5$ films irradiated with pico- and femtosecond laser pulses showed that full crystallization, including nucleation but primarily growth which is modelled here, occurs over time scales of nanoseconds.[6] This indicates that crystallization under short pulse irradiation proceeds after the removal of the laser pulse and during time scales commensurate of thermal relaxation in the GST layer.[14,15] Furthermore, the phonon mean free path length for amorphous and crystalline GST (assuming that the electronic contribution is small and using the thermal conductivity values in Table I along with the velocity of sound for GST in Ref. 16) is of the order 0.15 nm and 0.24 nm, respectively, which is smaller than the thickness of the GST film used in this work. Therefore, the transient temperature $T(r,z,t)$ within the GST film due to the application of the pump laser pulse may be described by the equilibrium and macroscopic heat conduction equation, which in one dimension is given by

$$\frac{1}{D}\frac{\partial T(z,t)}{\partial t} = \frac{\partial^2 T(z,t)}{\partial z^2} + \frac{g(r,z,t)}{k}, \quad (4)$$

in which z is the direction normal to the radial plane extending over r. The thermal diffusivity $D = k/\rho C_p$ where k, ρ and C_p are the thermal conductivity, density and heat capacity per unit mass respectively. Heat diffusion in the radial direction r is ignored following the assumption of one-dimensional (vertical) heat flow in the medium. The effects of the release of latent heat during crystallization and thermal anisotropies on the heat flow process are assumed negligible due to the small change in crystalline fraction during each femtosecond laser pulse (and their contribution is small for $Ge_2Sb_2Te_5$).[17] The source term, g, represents the transmitted power density of the pump laser beam in the GST layer and is derived using Poynting theorem in the Appendix. The transmission angle of the pump laser beam in the GST layer (incident at 43° and transmitted through the top ZnS:SiO$_2$ capping layer) was calculated to be $8° - 9°$ to the

TABLE I. List of thermal and kinetic parameters for the $Ge_2Sb_2Te_5$ and ZnS:SiO$_2$ layers used in the calculations.

Symbol	$Ge_2Sb_2Te_5$	ZnS:SiO$_2$	Units
ρ	5995[a]	3650[f]	kg/m³
C_p	218[b]	530[g]	J/(kgK)
k	0.23 (amor.)[c]	0.55[g]	W/(mK)
	0.53 (cryst. fcc)[c]		
	1.58 (cryst. hcp)[c]		
$\hat{n}$ (800 nm)	4.70 − j1.48 (amor.)[d]	2.13[h]	—
	5.17 − j3.34 (cryst. fcc)[d]		
	5.36 − j3.80 (cryst. hcp)[d]		
$\hat{n}$ (632 nm)	4.20 − j2.13 (amor.)[d]	2.15[h]	—
	3.80 − j3.67 (cryst. fcc)[d]		
	4.13 − j4.07 (cryst. hcp)[d]		
E_c	2.05[e]	—	eV
A_c	1.5×10^{22}[e]	—	s⁻¹
n	1, 3[e]	—	—

[a]Average density of amorphous and crystalline phases, Ref. 22.
[b]Dulong-Petit, high-temperature limit (>Debye temperature) for the molar heat capacity of GST at constant pressure, i.e., $C_p = 3Nk_B$ for 9 atoms of $Ge_2Sb_2Te_5$. Comparable values were measured for crystalline $Ge_2Sb_2Te_5$ at elevated temperatures in Ref. 24.
[c]References 16 and 25, room temperature values. The thermal conductivity of the crystalline material is for the fcc phase (expected in rapid annealing situations).
[d]Reference 18, values for 30 nm GST film sandwiched by 150 nm ZnS:SiO$_2$ films on a Silicon substrate. The amorphous refractive index is measured from the as-deposited film at room temperature, while the crystalline refractive index is measured at 150 °C with a cubic (fcc) phase.
[e]Within the range of published values in, for example, Refs. 2, 5, 20, and 22.
[f]Reference 26.
[g]Reference 24, measured at temperatures greater than the Debye temperature for ZnS.
[h]Reference 27.

normal for the crystalline and amorphous phases respectively. Therefore, it is legitimate to simplify the analysis by using normal transmission in the GST layer with power density

$$g(r,z,t) = q_0 \alpha n_2 |\tau_1 \tau_2|^2 \exp(-\alpha z)\exp(-2r^2/r_0^2)f(t), \quad (5)$$

where q_0 is the peak incident laser power per unit area, and $\alpha = 4\pi K_2/\lambda$ is the absorption coefficient of the GST layer with complex refractive index $\hat{n}_2 = n_2 - jK_2$ at wavelength λ. The transmission coefficients τ_1 and τ_2 at the air/ZnS:SiO$_2$ interface and at the ZnS:SiO$_2$/GST interface are given by $\tau_1 = 2/(1 + \hat{n}_1)$ and $\tau_2 = 2/(1 + \hat{n}_2/\hat{n}_1)$, respectively, where $\hat{n}_1$ is the (real) refractive index of the ZnS:SiO$_2$ capping layer, and $\hat{n}_2$ is the (complex) refractive index of the GST layer. The incident laser energy is assumed to have a circular Gaussian distribution for simplicity with $1/e^2$ radius equal to r_0. The function $f(t)$ describes the time profile of the pump laser pulse, and is assumed here to be a narrow square pulse of width t_w such that $\lim_{t_w \to 0} f(t) = t_w \delta(t)$, where $\delta(t)$ is the Dirac Delta function, thus producing a peak laser fluence of $E_0 = q_0 t_w$. This short pulse limit represents the instantaneous deposition of the experimental femtosecond pump laser energy and reduces the complexity of the solution of the heat conduction equation.

The experimental disk stack was modeled as two semi-infinite layers for simplicity (see Fig. 10 in the Appendix),

symmetrical about the interface $z = 0$ and therefore require the solution of two heat conduction equations matched at the interface. The top semi-infinite layer models limited flow and storage of heat through the 30 nm ZnS:SiO$_2$ capping layer and air, with a thermally insulating boundary at $z \rightarrow -\infty$. The lower semi-infinite layer models heat flow through the GST layer, ZnS:SiO$_2$ underlayer and the high thermal conductivity Si substrate with the boundary at $z \rightarrow \infty$ approaching room temperature T_0. The source term g in Eq. (5) extends only over part of the lower semi-infinite layer, equivalent to thickness of the GST layer ($d = 20$ nm), where optical absorption of the incident pump beam takes place (the optical absorption depth $\Delta = 1/\alpha$ at 800 nm was calculated using the optical constants in Table I, and found to exceed the thickness of the GST layer for both the amorphous and crystalline phases). The remainder of the lower semi-infinite structure has the same thermal parameters of GST and is used to approximately model the thick (310 nm) ZnS:SiO$_2$ underlayer (with similar thermal parameters to GST). Thermal boundary resistance between the GST layer and ZnS:SiO$_2$ capping/underlayer is not included in the model to reduce the mathematical complexity, but its influence is implicitly present through the large thicknesses of the capping and underlayers in the model. Absorption of the

optical energy in the Si substrate and possible crystallization of the dielectric ZnS:SiO$_2$ layers[18] are not modelled in this work to reduce the mathematical complexity of the problem and is beyond the remit of this work. However, the effect of energy absorption in the Si substrate is expected to be small due to the relatively large thickness of the dielectric underlayer. The two-layer system is solved analytically in the Appendix using Laplace transforms, and the closed-form solution yielded very good agreement with more detailed finite-element calculations of the temperature in the complete experimental stack. The calculated transient temperature in the GST layer from this theory is used next in the calculation of the crystalline volume fraction.

The thermally activated increase of the crystalline volume fraction χ is described here for simplicity by the rate equation[19]

$$\frac{\partial \chi(r,z,t)}{\partial t} = A_c (1 - \chi(r,z,t))^n \exp\left(\frac{-E_c}{k_B T(r,z,t)}\right), \quad (6)$$

in which A_c is the attempt frequency and E_c the height of the energy barrier (or effective activation energy for crystallization), n is the reaction order, and k_B is Boltzmann's constant. The solution to this rate equation has the form:

$$1 - \chi(r,z,t) = (1 - \chi_0)\exp\left\{-A_c \int_{t'=0}^{t} \exp\left(\frac{-E_c}{k_B T(r,z,t')}\right)dt'\right\} \qquad n = 1,$$

$$1 - \chi(r,z,t) = \left\{(1 - \chi_0)^{(1-n)} + A_c(n-1) \int_{t'=0}^{t} \exp\left(\frac{-E_c}{k_B T(r,z,t')}\right)dt'\right\}^{\frac{1}{(1-n)}} \qquad n \neq 1,$$

$$(7)$$

in which χ_0 is the crystalline fraction prior to the arrival of the optical pulse. Equation (7) can be easily solved by rewriting the integral as a convolution with the unit-step function $U(t-t')$:

$$\int_{t'=0}^{t} \exp\left(\frac{-E_c}{k_B T(r,z,t')}\right)dt' = \int_{t'=0}^{\infty} \exp\left(\frac{-E_c}{k_B T(r,z,t')}\right)U(t - t')dt'$$

and carrying out the integration using the fast-Fourier transform (FFT). More detailed rate equation models consider both the stabilization of crystalline nuclei of critical size and their subsequent growth.[20] However, in the present case, Eq. (7) will be applied after an initial incubation period, which, from inspection of Fig. 4, is taken to be about 150 pulses.

The effective reflection coefficient Γ_t for illumination from the white light source of the microscope at normal incidence is approximated by

$$\Gamma_t = \Gamma_1 + \Gamma_2 + \Gamma_1 \Gamma_2, \quad (8)$$

which only includes contributions of the reflected fields from the air/ZnS:SiO$_2$ interface ($\Gamma_1 = (1 - \hat{n}_1)/(1 + \hat{n}_1)$) and

from the ZnS:SiO$_2$/GST interface ($\Gamma_2 = (1 - \hat{n}_2/\hat{n}_1)/(1 + (\hat{n}_2/\hat{n}_1))$), assuming for simplicity that reflections from deeper layers have negligible effect. The reflectance R is then calculated from $R = |\Gamma_t|^2$.

The relative permittivity of the GST layer, ε, is related to the complex refractive index, $\hat{n}$, by $\sqrt{\varepsilon} = \hat{n}$. From effective medium theory, the complex relative permittivity for a mixture of amorphous and crystalline material with volume fractions $(1 - \chi)$ and χ, respectively, can be determined according to[21]

$$\varepsilon(\chi, \varepsilon_{am}, \varepsilon_{cr}) = \frac{1}{4}(\gamma \pm \sqrt{\gamma^2 + 8\varepsilon_{am}\varepsilon_{cr}}), \quad (9)$$

where $\gamma = (3(1 - \chi) - 1)\varepsilon_{am} + (3\chi - 1)\varepsilon_{cr}$ and ε_{am} and ε_{cr} are the permittivities of the amorphous and crystalline phases, respectively. Equation (9) is used to update the complex refractive index in the GST layer in the heat source term in Eq. (5) after each pump pulse (at 800 nm), and to calculate the corresponding optical reflectance (at 632 nm) in Eq. (8). The value of the thermal conductivity k for the partially crystallized film is also assumed to evolve as a volume

weighted average of the values for the amorphous and crystalline states with each laser pulse. The heat capacity does not change appreciably over a wide temperature range and is taken as constant (see Table I).

A. Simulation results

Calculations have been performed for a circular pump spot of Gaussian profile with $1/e^2$ radius $r_0 = 37 \ \mu m$ and with $1/e^2$ area equal to the elliptical pump beam area determined with the beam profiler. Table I lists the material parameters used in the calculations. The energy barrier height was varied within published values until good agreement was obtained with experiment. The reaction order (equivalent to the Avrami exponent from the JMA theory for isothermal annealing) is often associated with the crystallization mechanism[22] but with uncertainties regarding its interpretation particularly under non-isothermal annealing conditions and is therefore not discussed here.[23] The reaction orders used in the calculations ($n = 1, 3$), which are within published values, are intended to illustrate the effect of this parameter on the crystallization kinetics and the calculated reflectivity and mark areas.

Initial theoretical temperature calculations were carried out using a two-dimensional, depth average heat diffusion model (not included in this paper) and revealed negligible heat flow in the radial direction during femtosecond laser irradiation and on the scale of the spot radius, justifying the use of the one-dimensional heat conduction equation. The solution of Eq. (4) is valid only for temperatures less than the melting temperature of 894 K for GST[28] and assumes that the optical and thermal parameters of the GST material do not vary with thickness. Figures 6(a) and 6(b) show the calculated temperature distribution through the amorphous phase-change layer at different times using $F_{avg} = 2.33$ mJ/cm^2. It can be seen that the temperature is maximum imme-

diately after the optical excitation near the upper surface of the GST layer ($z = 0$ nm), before diffusing through the adjacent layers. Therefore crystallization is expected to first occur through heterogeneous nucleation at the GST/ZnS:SiO$_2$ capping interface.[22] The remaining 20 nm of the GST film can then crystallize by growth from the upper surface of the film with increasing laser pulse number. Nucleation and growth deeper within the GST layer is also expected to occur with each subsequent pulse, since the optical absorption depth at the pump laser wavelength extends over the full thickness of the GST film. The full extent of the optical absorption through the phase-change layer thickness also leads to the initial small temperature gradient through this layer as shown in Fig. 6(a), after which the maximum temperature tends towards the centre of the layer as time proceeds. With increasing laser pulse number, the amorphous layer gradually crystallizes leading to increased optical absorption (due to the increase in extinction coefficient as shown in Table I) and therefore higher surface temperatures as illustrated in Figs. 6(b) with a larger temperature gradient through the layer thickness. Surface melting can thus occur with increasing pulse number even at modest fluences, and the final phase after quenching would be determined by factors such as the melt depth, the cooling rate and the phase of the surrounding material as will be discussed later.

The calculated transient temperatures at different depths through the phase-change layer are shown in Figs. 6(c) and 6(d) for the amorphous and crystalline phases, respectively. The contact of the GST layer with the ZnS:SiO$_2$ capping and under-layers leads to heat extraction and therefore lower temperatures near these interfaces with the maximum temperature occurring in the centre of the medium as time progresses. While the contact with the underlayer influences thermal relaxation after few nanosecond from the removal of the femtosecond laser pulse over diffusion lengths equal to the GST layer thickness, heat diffusion and storage through
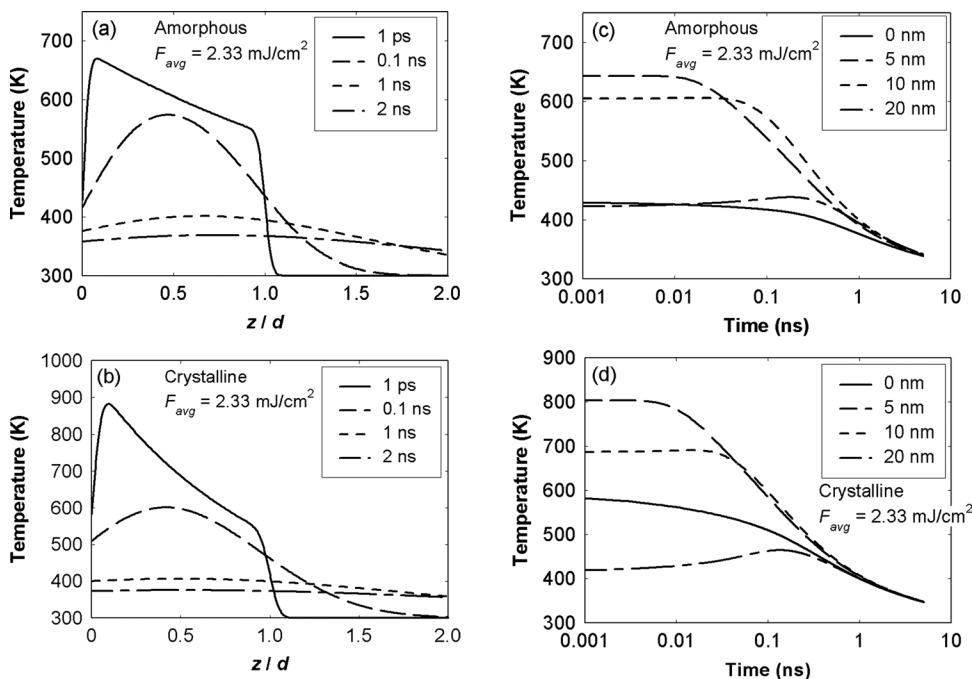

FIG. 6. Calculated transient temperature distributions using the analytical model derived in this work for applied pump fluence of $F_{avg} = 2.33$ mJ/cm^2 over 60 fs. Plots (a) and (b) show the temperature distribution through the GST layer as a function of normalised thickness at different times when fully amorphous and fully crystalline respectively. Plots (c) and (d) are the calculated the transient temperatures at different points through the 20 nm thick, fully amorphous and fully crystalline GST layer respectively.

the capping layer happens immediately after the removal of the laser pulse leading to reduction in the surface temperature and rate of cooling at short time scales as indicated in Figs. 6(c) and 6(d).

The temperature in the centre of the phase-change layer ($z = 10$ nm) is used conveniently as a thickness averaged temperature to evaluate a depth averaged crystalline volume fraction in the GST layer from Eq. (7). The phase-change medium is taken to be amorphous initially with crystalline volume fraction $\chi_0 = 0$, and updates after every subsequent pulse using Eq. (7). Calculations of the crystalline volume fraction for fluences below the melt and damage threshold confirmed that it is not possible to crystallize the heated region using a single 60 fs pulse in agreement with experiment. Applying successive fs laser pulses and with increasing fluence (below the melt threshold) increase the calculated crystalline fraction and corresponding reflectance. The continuous and dashed lines in Fig. 3(c) represent the calculated change in reflectance $\Delta R/R_{am}$ with increasing F_{avg} after 2000 pulses, illustrating a sharp increase in reflectance reaching a maximum of 24% at an average fluence of 2.8 mJ/cm^2, in good agreement with the experimental measurements at the centre of the crystalline mark. The calculated reflectance change in Fig. 3(c) is slightly lower than the experimental values at the centre of the mark. This may be attributed to ignoring the contributions of the reflected waves from the underlayer/substrate interface in the experimental stack in evaluating the reflection coefficient from Eq. (8), and/or the variations of optical constants through the thickness of the phase-change layer (which is not accounted for in the present model) and in the literature.

It is assumed in the calculations that the GST layer remains amorphous if the maximum calculated temperature at the centre of the film reaches the melting point after the application of the first laser pulse (i.e., re-amorphization). This indicates the onset of the melting threshold in the centre of the heated region and formation of the observed annular crystalline rings. This occurred when $F_{avg} = 4.66$ mJ/cm^2 and is marked by the sharp drop in the calculated value of $\Delta R/R_{am}$ from 24% to 0% as shown in Fig. 3(c), in close agreement with the reflectivity measurements (black circles in Fig. 3(c)). This melting threshold value also agrees with the fluence determined from the geometrical fitting of the laser beam profile to the crystalline mark area (4.77 mJ/cm^2) where the area reaches its maximum (saturation) value in Fig. 3(d) due to the formation of annular crystalline rings with amorphous centres.

Evaluating the one-dimensional temperature at different radial locations enables the determination of the area of the crystallized region for a given fluence and pulse number. The theoretical areas were determined from the radius at 50% of the maximum calculated crystalline fraction distribution of the mark and are plotted as a function of increasing average fluence after 2000 pulses in Fig. 3(d) (dashed lines). The calculated areas are in very good agreement with the measurements and fittings to the laser beam profile in Eq. (2), predicting accurately the measured melting threshold near $F_{avg} = 4.66$ mJ/cm^2 (inflection point on curve and onset of appearance of annular crystalline rings in Fig. 2). The cal-

culated area for a fixed laser fluence (below the melting threshold) as a function of pulse number is shown in Fig. 4(b) and follows closely the experimental increase in area with increasing pulse number. This close agreement further confirms that the crystalline mark area is primarily determined by the incident laser beam profile rather than lateral heat diffusion and supports the one-dimensional (vertical) heat flow model proposed in this paper.

Returning to the experimental reflectivity curves in Fig. 4(c), the gradual increase in crystalline fraction with successive laser pulses increases the optical reflectance and provides a means of following the crystallization kinetics. It can be noticed from this figure that the change in reflectance with increasing pulse number after the incubation period (and hence crystallization rate) is less sensitive to the applied fluence. This behaviour was observed in transient reflectivity measurements of 200 nm GST films irradiated with isolated pico-second laser pulses at increasing fluence.[15] The crystallization rate depends on the peak temperature in the medium (and hence peak laser fluence), the cooling rate, the activation energy for crystallization, and the crystallization mechanism (which may be described by the reaction order of the system). This complex dependence may be approximated by assuming that the decrease in temperature after the application of a laser pulse can be described by

$$T = T_P(1 - \phi t),$$

with constant cooling rate $T_P\phi$, where T_P is the peak temperature in the film (determined by the peak laser fluence) and ϕ is the cooling rate parameter (related only to the thermophysical parameters in the structure). Substituting this temperature in the rate equation (6) and evaluating the crystallization rate at small times yields the approximation

$$\frac{d\chi}{dt} \approx A_c (1 - \chi(0))^n \exp\left(\frac{-E_c}{k_B T_P}\right). \qquad (10)$$

Equation (10) reveals that the crystallization rate should increase with increasing peak temperature (and therefore fluence), and this is confirmed from the theoretical calculations shown in Fig. 4(d) using the crystallization model in this paper. This dependence of crystallization rate on laser fluence is not visible in the experimental curves in Fig. 4(c). This may be caused by the increase in optical absorption with increasing crystalline fraction with consecutive laser pulses, raising the temperature in the GST layer to near melting (see Fig. 6(c)) and therefore decreasing the crystalline growth rate. Alternatively, surface melting can take place with increasing crystalline fraction at moderately low fluences due to increased optical absorption as indicated in Fig. 7. Solidification of the melt in this case (at T_m) will occur at a cooling rate independent of the pump laser fluence and determined mainly by the thermophysical parameters of the layers in the stack leading to an approximately constant recrystallization rate independent of the laser fluence.

The values of E_c and A_c used here are similar to those deduced from other studies, demonstrating that fs writing experiments provide an easy and reliable means of characterizing and quantifying crystallization kinetics. The large value
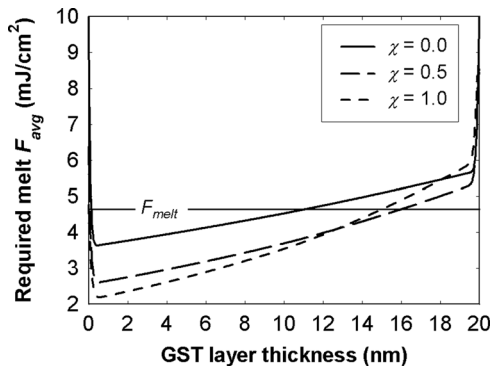
FIG. 7. Calculated average fluence F_{avg} (for a single laser pulse) required to induce melting at the centre of the irradiated region at increasing depths into the GST layer for different crystalline volume fractions. The melting threshold fluence F_{melt} is indicated at the average fluence of 4.66 mJ/cm² observed from measurements and calculations in Figs. 3(c) and 3(d). $z = 0$ nm corresponds to the surface of the GST layer. The required fluence for melting was calculated using the theoretical heat flow model which does not account for melting and movement of the melting front. This leads to the exaggerated large values of F_{avg} near the capping and under-layers ($z = 0$ and 20 nm respectively). In practice, the melting front would reach and make contact with these interfaces.

of A_c, which appears unphysical, is a consequence of ignoring the distribution of energy barriers that must be included within a more detailed model.[29]

V. DISCUSSION

The use of femtosecond laser pulses to crystallize phase-change material is an attractive route for increasing the erase speed in optical disk systems, with less stringent requirements on the thermal layers in the disk stack. This is possible because crystallization and mark formation are determined by the instantaneous deposition of laser energy rather than heat diffusion, and the ability to tailor the number of pulses in addition to the laser fluence to control the crystallization process within a given disk structure. Controlling the number of excitations has been shown to further extended the functionality of phase-change media to arithmetic, logic and biologically inspired computations.[30]

To understand the complex dependence of the laser fluence and pulse number on the observed formation of full crystalline marks and annular rings in the GST film (shown in Fig. 4(a)), two regimes will be considered based on the magnitude of the applied fluence in comparison to the observed melting threshold fluence F_{melt} (~4.66 mJ/cm² for the experimental stack used in this work). These two regimes are illustrated in Fig. 7 which shows the calculated fluence required to melt a certain location through the thickness of the GST film for different levels of crystallization. The required melting fluence was determined by solving $T_m = T(0, z, t_m)$ for E_0 at different locations z through the thickness of the GST layer and at the centre of the laser beam ($r = 0$). T is the theoretical temperature determined from the solution of the heat conduction equation, T_m is the melting temperature (894 K) and t_m is the time taken for the temperature to reach its maximum value at a given location z, which was calculated numerically using the theoretical temperature from the Appendix.

In the first regime at fluences less than the melting threshold, for example, $F_{avg} = 2.33$ mJ/cm², the temperature is maximum near the surface of the GST layer as shown in Fig. 6, with values between the glass transition and melting temperatures sufficient to induce crystallization. Subsequent irradiation of the same area with femtosecond laser pulses gradually increases the crystalline fraction and optical reflectivity leading to the formation of full crystalline marks as shown in Fig. 2 after 2000 pulses. The theoretical plot in Fig. 7 shows that no melting takes place at this low fluence in the amorphous starting phase, leading to solid-state crystallization of the irradiated region and confirming the observed formation of full crystalline marks.

Increasing the applied laser fluence to ~3.7 mJ/cm² increases the temperature in the surface of the GST layer (at the centre of the irradiated region) causing melting of the amorphous starting material ($\chi = 0$) as shown in Fig. 7. Direct contact of the molten material to the capping layer and efficient heat extraction would result in fast cooling and quenching to the amorphous phase in the surface area of the GST layer and at the centre of the irradiated region. The surrounding region experiences lower temperatures and crystallize gradually with increasing pulse number thus forming the crystalline annular rings observed in Fig. 4(a). The annular crystalline rings start to be visible at fluences ≥3.50 mJ/cm² in Fig. 4(a) which agree with the fluence of 3.7 mJ/cm² predicted in Fig. 7 for the onset of surface melting from the amorphous starting phase. Applying successive laser pulses to the same region leads to closure of the crystalline annular rings and formation of complete crystalline marks as shown in Fig. 2 after 2000 pulses. The crystalline material in this case can grow from the inner perimeter of the mark and from the crystalline material embedded within the volume of the GST layer,[31] either directly from the melt or more likely when the material has solidified and the temperature remains above the glass transition temperature. This is supported by the existence of nucleation centres created in the melt-quenched central amorphous region after the application of tens of laser pulses, enhancing growth upon cooling.[32–34] The release of heat of fusion during solidification of the melt, the thick underlayer and thermal boundary resistance also work to reduce the cooling rate and promote recrystallization of the melt.[35] The line scans in Figs. 3(a) and 3(b) showed an increase in ΔR at the outer perimeter of the crystalline marks (≥30%) compared to the centre of the mark (~25%). This increase in ΔR most likely indicates the formation of the hexagonal crystalline phase resulting from the high temperatures (<melting) experienced in the outer regions of the mark from successive laser pulses, leading to solid-state gradual solid-state crystallization without melting. Calculations of the reflection coefficient in Eq. (8) using the optical constants for GST listed in Table I at 632 nm yield changes in reflectance $\Delta R/R_{am}$ of 24% and 32% for the fcc and hcp crystalline phases, respectively, in agreement with the microscope reflectivity measurements. The possible existence of the hexagonal phase in the surrounding crystalline material may also contribute to enhancing the recrystallization of the melt-quenched central region when surface melting occurs.[36] The melt-quenched central region
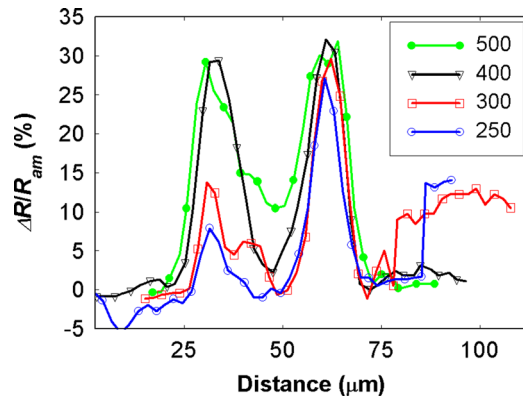
FIG. 8. Reflectance line scans along the semi-major axis of the marks shown in Fig. 4(a) produced using different number of 85 femtosecond pulses at $F_{avg} = 4.20$ mJ/cm^2 showing the growth of the crystalline material from the inner perimeter and central region of the annular rings with increasing pulse number.

re-crystallizes to the fcc crystalline phase.[36] Figure 8 shows reflectance line scans along the semi major-axis of marks written at $F_{avg} = 4.20$ mJ/cm^2 from Fig. 4(a) indicating crystal growth from the inner perimeter and central region of the marks with increasing pulse number, supporting the above re-crystallization model. It is important to note that re-crystallization or closure of the ring structures happened here over a relatively large number of pulses (hundreds). This is because surface melting started in the as-deposited amorphous material upon the application of the first laser pulse with no pre-crystallized boundaries to promote fast growth, and absence of nucleation centres in the volume of the as-deposited amorphous film which required hundreds of pulses to create (equivalent to the incubation time).

Successive laser pulses at fluences less than F_{melt} increases the crystalline volume fraction in the GST film (and hence reflectance), subsequently increasing the absorption of optical laser energy and temperature in the film. This increase in temperature reduces the average fluence needed to melt the GST film as indicated in Fig. 7 for $\chi > 0$. Therefore, it is expected that melting of the central region of crystalline marks may occur at average fluences less than the melting threshold F_{melt} with increasing pulse number. Re-crystallization of the melt-quenched material and closure of the annular rings is expected to take place at a faster rate in this case with fewer successive pulses, through growth from the pre-existing crystalline boundary and within the volume of the film.

The second regime considered here for studying crystallization by successive fs pulses is identified by fluences greater than or equal to the melt threshold of $\sim$4.66 mJ/cm^2. At these fluences, the melting temperature isotherm extends deeper through the GST film thickness as shown in Fig. 7. The melting front will move to make contact with the capping and underlayer to provide efficient heat extraction and therefore high cooling rates for the melt to quench to the amorphous phase. This is evident from the formation and persistence of annular crystalline rings with amorphous centres even after the application of 2000 laser pulses at fluences $\geq F_{melt}$ as indicated in Fig. 2. If annular crystalline rings were formed with the hexagonal phase, as implied by

the high reflectance measurement in this region, then their high thermal conductivity will further insure efficient removal of heat upon solidification to the surrounding amorphous phase. Applying fluences higher than F_{melt} will cause melting through the complete GST film followed by cooling and quenching to the amorphous phase through contact and efficient heat extraction through the capping and underlayers, and therefore erasure of the crystalline marks, as demonstrated in Fig. 5.

The theoretical analysis presented in this paper relied on using the heat conduction equation to explain the formation of crystalline marks after the application of femtosecond pulses, based on the assumption that crystallization occurs during thermal relaxation at equilibrium time scales, and the small phonon mean free path length compared to the GST film thickness. This theory produced good agreement with the experimental observation and was successful in predicting the reflectance levels and melt threshold fluences that were observed from measurements, and went some way into explaining the formation of crystalline marks and annular structures. We have also carried out other pump-probe measurements on the same sample used in this work using successive laser pulses having widths of 500 fs and 2 ps. Crystalline marks and annular rings were also formed in these experiments with mark dimensions and reflectivities exhibiting almost identical dependence on the laser fluence and pulse number that are reported in this work. This would indicate that the same crystallization mechanisms are in operation at these time scales and implies the validity of using the one-dimensional, thermal equilibrium theory to explain some aspects of thermal transport and crystallization in the phase-change medium under femtosecond laser excitation. Non-thermal effects may be present; particularly non-thermal melting and amorphization under femtosecond laser excitation.[34,37] Confirmation of their influence would require transient reflectivity and structural measurements which will form the scope of future investigations.

The reduction of inner perimeters of marks in Fig. 4(a) for fluences 4.20 mJ/cm^2 and 4.43 mJ/cm^2 is plotted in Fig. 9 against pulse number. The straight-line fits shown in Fig. 9 estimate growth velocities in the range 7–9 m/s, assuming that crystal growth, or amorphous-to-crystalline interface displacement, after each fs pulse reaches the steady-state within 2 ns estimated from the time taken for the temperature (at $z = 10$ nm) to decrease from the melting point to the glass transition temperature $T_g \sim 400$ K.[27,38] There was negligible change in the outer diameters of the marks at these fluences. While there is potential for further refinement of this measurement technique since the medium experiences different temperatures at different locations of the mark, this estimate is in good agreement with the 10 m/s growth rate obtained from low temperature differential scanning calorimetry (DSC) measurements extrapolated to high temperatures near the melting point,[27] and upper bound estimates of diffusion limited growth velocity of 13.5 m/s from fitting to ultra-high speed DSC measurements.[38] The estimated crystal growth velocities in this work are higher than the current reported value of 3 m/s measured using ultrafast-heating calorimetry at a heating rate of 4×10^4 K/s at 0.72 T_m on an 80 nm thick,
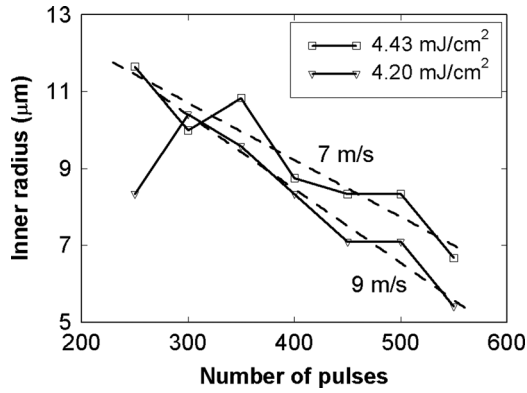
FIG. 9. Measurements of the inner diameters of the annuli in Fig. 4(a) for two fluences as functions of increasing laser pulse number. The straight lines fits reveal an estimate of the elevated temperature growth velocity assuming that the growth occurs over a 2 ns period from the application of a laser pulse, during which the maximum temperature reduces to the glass-transition temperature and the amorphous-to-crystalline interface displacements is at its steady-state value.

amorphous GST film without a capping layer.[38] The existence of pre-crystallized/primed annular crystalline rings formed by the fs laser annealing are therefore expected to enhance and increase the crystal growth velocity in this work at higher temperatures. Moreover, it is also important to realise that growth in this work happens during cooling from high temperatures (either through melt-quenched re-crystallization or through solid-state crystallization) at high and non-constant rates, which is different from calorimetry experiments where crystallization happens gradually from the amorphous start phase during ramping of the temperature from low values at a fixed heating rate. Thus, it is expected that the crystallization (or growth) kinetics will be different for both cases.

VI. CONCLUSIONS

We have conducted a comprehensive investigation of how the crystallization of amorphous $Ge_2Sb_2Te_5$ thin films may be achieved with multiple amplified femtosecond laser pulses of varying fluence. By using a spot size of tens of microns and performing an accurate characterization of the spot profile we have been able to examine the effect of a continuous range of local fluence. We observed that the as-deposited amorphous $Ge_2Sb_2Te_5$ films could not be crystallized using a single pulse and that larger fluences led first to melting and re-amorphization and then to irreversible damage. For fluences below the damage threshold, a minimum of about 200 pulses was required to induce crystallization. Typically the crystalline mark was of annular shape, with the fluence at the centre of the mark being sufficient to induce melting. A solid elliptical mark was only achieved for smaller fluences. For a fixed number of pulses, the dependence of the area of the crystalline mark upon the pump fluence is well described by simple algebraic results that fully justify the assumption that thermal transport within the sample is one-dimensional (vertical). A model has been presented in which consideration of the optical absorption, thermal transport and thermally activated crystallization

leads to simulations of the evolution of the optical reflectivity and mark area that are in good quantitative agreement with the experimental data. Indeed, the simulations yield reasonable values of the activation energy and attempt frequency. The analysis of marks made by amplified fs pulses therefore provides a new and effective means of understanding the crystallization of phase change materials. Finally, the closure of crystalline annular rings, formed from melt-quenching the centres of marks to the amorphous phase, with successive laser pulses provides a potentially useful and indirect method of estimating the growth rate of phase-change materials at high temperatures, and was estimated in this work for $Ge_2Sb_2Te_5$ to be in the range 7–9 m/s.

APPENDIX: OPTICAL ABSORPTION AND TEMPERATURE DISTRIBUTION IN THE PHASE-CHANGE LAYER

The power density in (W/m^3) generated in the phase-change layer due to the applied pump laser is determined from the normalised divergence of the time-averaged transmitted power in the phase-change layer per unit area $\langle \bar{S}_2 \rangle$:

$$\text{Re} \left\{ -\nabla . \frac{\langle \bar{S}_2 \rangle}{\langle \bar{S}_i \rangle} \right\},$$

where $\langle \bar{S}_i \rangle$ is the time-averaged power density of the incident laser beam (in air). Evaluating the power densities using Poynting's theorem assuming the incident medium is lossless yields

$$\text{Re} \left\{ -\nabla . \frac{\langle \bar{S}_2 \rangle}{\langle \bar{S}_i \rangle} \right\} = \alpha \frac{n_2}{n_i} \frac{|\bar{E}_2|^2}{E_i^2}, \qquad (A1)$$

where $\bar{E}_2$ is the transmitted electric field in the phase-change layer and E_i is the magnitude of the incident electric field. n_i and n_2 are the real parts of the refractive indices in the incident (air) and transmitted (phase-change) media, respectively, and α is the optical absorption coefficient in the phase-change layer. For normal incidence, the transmitted electric field along the z-direction may be written as:

$$|\bar{E}_2|^2 = |\tau_1 \tau_2|^2 E_i^2 \exp(-\alpha z),$$

where τ_1 and τ_2 are the transmission coefficients at the air/ZnS:SiO$_2$ and ZnS:SiO$_2$/GST interfaces, respectively. Substituting the transmitted electric field in Eq. (A1) noting that $n_i = 1$ provides the normalized power as:

$$\text{Re} \left\{ -\nabla . \frac{\langle \bar{S}_2 \rangle}{\langle \bar{S}_i \rangle} \right\} = \alpha n_2 |\tau_1 \tau_2|^2 \exp(-\alpha z).$$

Multiplying by the incident laser beam power per unit area q_0 with an assumed Guassian distribution of $1/e^2$ radius r_0, and time profile $f(t)$ provides the power density source term needed for determining the transient temperature in the phase-change layer

$$g(r,z,t) = q_0 \alpha n_2 |\tau_1 \tau_2|^2 \exp(-\alpha z)\exp(-2r^2/r_0^2)f(t). \quad (A2)$$

The experimental stack is modeled approximately using the two semi-infinite layers shown in Fig. 10, symmetrical about $z = 0$. Heat is generated within the bottom layer due to the incident laser beam over the thickness d of the GST layer with energy density g. This results in vertical heat flow and storage through the top ZnS:SiO$_2$ capping layer and down through the thick ZnS:SiO$_2$ underlayer towards the Si substrate. The temperatures in the two semi-infinite layers are determined from solution of the heat conduction equations:

$$\frac{1}{D_1}\frac{\partial T_1}{\partial t} = \frac{\partial^2 T_1}{\partial z^2} + \frac{g(r,z,t)}{k_1}, \quad (A3)$$

$$\frac{1}{D_2}\frac{\partial T_2}{\partial t} = \frac{\partial^2 T_2}{\partial z^2}. \quad (A4)$$

Using the narrow pulse limit for the time profile of the laser pulse in g with $f(t) = t_w \delta(t)$, applying the Laplace transform with respect to time t to the partial differential equations, and solving using the boundary conditions described in Fig. 10 yields the solutions:

$$T_1(r,z,s) - T_0 = Be^{\mu_1 z} - \frac{g'}{2k_1}\frac{e^{-\alpha d}e^{\mu_1(z-d)}}{\mu_1(\mu_1+\alpha)} + \frac{g'}{k_1}\frac{e^{-\alpha z}}{(\mu_1^2-\alpha^2)}, \quad (A5)$$

$$T_2(r,z,s) - T_0 = Ce^{\mu_2 z}, \quad (A6)$$

where s is the Laplace operator, $\mu_1 = \sqrt{s/D_1}$, $\mu_2 = \sqrt{s/D_2}$, and g' is given by
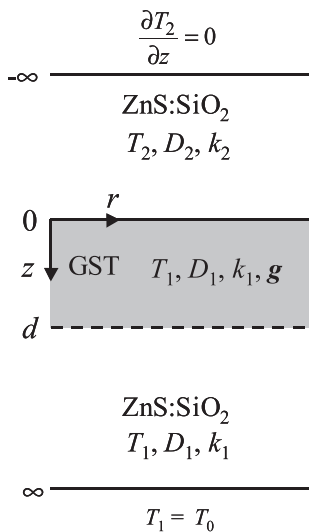

FIG. 10. Diagram illustrating the two-layer, semi-infinite model of the experimental stack used for evaluating the temperature distribution T_1 in the GST layer. The laser beam energy absorption, identified by the power density term g, is limited to the thickness of the GST layer d.

$$g'(r,z,s) = E_0 \alpha n_2 |\tau_1 \tau_2|^2 \exp(-\alpha z)\exp(-2r^2/r_0^2),$$

where $E_0 = q_0 t_w$. The constants of the integration B and C are determined by applying the continuity of temperatures and heat flux conditions:

$$T_1 = T_2, \quad k_1 \frac{dT_1}{dz} = k_2 \frac{dT_2}{dz},$$

at the interface $z = 0$. The inverse Laplace transform can be determined exactly yielding the closed-form solution for the temperature in the GST layer:

$$\begin{aligned}
T_1(r,z,t) - T_0 = {} & \frac{g'D_1}{2k_1}e^{\alpha^2 D_1 t}e^{-\alpha z} \\
& \times \left\{ 2 - Erfc\left(\frac{d-z}{2\sqrt{D_1 t}} + \alpha\sqrt{D_1 t}\right) \right. \\
& \quad - Erfc\left(\frac{z}{2\sqrt{D_1 t}} - \alpha\sqrt{D_1 t}\right) \\
& \quad - \eta e^{2\alpha z}\left[Erfc\left(\frac{d+z}{2\sqrt{D_1 t}} + \alpha\sqrt{D_1 t}\right) \right. \\
& \quad \left.\left. - Erfc\left(\frac{z}{2\sqrt{D_1 t}} + \alpha\sqrt{D_1 t}\right)\right] \right\} \quad (A7)
\end{aligned}$$

where $Erfc$ is the complementary error function and η is given by

$$\eta = \frac{k_1/k_2\sqrt{D_2/D_1} - 1}{k_1/k_2\sqrt{D_2/D_1} + 1}.$$

[1]*Phase Change Materials: Science and Applications*, edited by S. Raoux and M. Wuttig (Springer, 2008).

[2]N. Yamada, E. Ohno, K. Nishiuchi, N. Akahira, and M. Takao, J. Appl. Phys. **69**, 2849 (1991).

[3]J. Solis and C. N. Afonso, Phys. Rev. Lett. **76**, 2519 (1996).

[4]N. Yamada and T. Matsunaga, J. Appl. Phys. **88**, 7020 (2000).

[5]V. Weidenhof, I. Friedrich, S. Ziegler, and M. Wuttig, J. Appl. Phys. **89**, 3168 (2001).

[6]J. Siegel, A. Schropp, J. Solis, C. N. Afonso, and M. Wuttig, Appl. Phys. Lett. **84**, 2250 (2004).

[7]J. Siegel, W. Gawelda, D. Puerto, C. Dorronsoro, J. Solis, C. N. Afonso, J. C. G. de Sande, R. Bez, A. Pirovano, and C. Wiemer, J. Appl. Phys. **103**, 023516 (2008).

[8]C. H. Chu, C. D. Shiue, H. W. Cheng, M. L. Tseng, H. P. Chiang, M. Mansuripur, and D. P. Tsai, Opt. Express **18**, 18383 (2010).

[9]S. M. Huang, Z. Sun, C. X. Jin, S. Y. Huang, and Y. W. Chen, Trans. Nonferrous Met. Soc. China **16**, Supplement 1, s226–s231 (2006).

[10]K. Sokolowski-Tinten, J. Solis, J. Bialkowski, J. Siegel, C. N. Afonso, and D. von der Linde, Phys. Rev. Lett. **81**, 3679 (1998).

[11]B. S. Lee, G. W. Burr, R. M. Shelby, S. Raoux, C. T. Rettner, S. N. Bogle, K. Darmawikarta, S. G. Bishop, and J. R. Abelson, Science **326**, 980 (2009).

[12]G. Zhang, F. Gan, S. Lysenko, and H. Liu, J. Appl. Phys. **101**, 033127 (2007).

[13]T. Ohta and H. Yamamoto, in *Proceedings of the European Symposium on Phase Change and Ovonic Science*, Switzerland, 2001.

[14]M. M. Aziz, M. R. Belmont, and C. D. Wright, J. Appl. Phys. **104**, 104912 (2008).

[15]K. Zhang, S. Li, G. Liang, H. Huang, Y. Wang, T. Lai, and Y. Wua, Physica B **407**, 2447 (2012).

[16]H. Lyeo, D. G. Cahill, B. Lee, and J. R. Abelson, Appl. Phys. Lett. **89**, 151904 (2006).

[17]M. Belmont, M. M. Aziz, and C. D. Wright, J. Appl. Phys. **104**, 044901 (2008).

[18]A. Chabli, C. Vergnaud, F. Bertin, V. Gehanno, B. Valon, B. Hyot, B. Bechevet, M. Burdin, and D. Muyard, J. Magn. Magn. Mater. **249**, 509 (2002).

[19]H. E. Kissinger, Anal. Chem. **29**, 1702 (1957).

[20]S. Senkader and C. D. Wright, J. Appl. Phys. **95**, 504 (2004).

[21]R. Landauer, AIP Conf. Proc. **40**, 2 (1978).

[22]N. Ohshima, J. Appl. Phys. **79**, 8357 (1996).

[23]M. C. Weinberg, D. P. Birnie III, V. A. Shneidman, J. Non-Cryst. Solids. **219**, 89 (1997).

[24]M. Kuwahara, O. Suzuki, Y. Yamakawa, N. Taketoshi, T. Yagi, P. Fons, T. Fukaya, J. Tominaga, and T. Baba, Jpn. J. Appl. Phys. **46**, 3909–3911 (2007).

[25]E. Kim, S. Kwun, S. Lee, H. Seo, and J. Yoon, Appl. Phys. Lett. **76**, 3864 (2000).

[26]T. Ohta, K. Inoue, M. Uchida, K. Yoshioka, T. Akiyama, S. Furukawa, K. Nagata, and S. Nakamura, Jpn. J. Appl. Phys. **28** (sup 28–3), 123 (1989); available at http://jjap.jsap.jp/link?JJAPS/28S3/123/.

[27]E. R. Meinders, A. V. Mijiritskii, L. van Pieterson, and M. Wuttig, *Optical Data Storage: Phase-Change Media and Recording* (Springer, 2006).

[28]J. Kalb, F. Spaepen, and M. Wuttig, J. Appl. Phys. **93**, 2389 (2003).

[29]D. Ielmini and M. Boniardi, Appl. Phys. Lett. **94**, 091906 (2009).

[30]C. D. Wright, Y. Liu, K. I. Kohary, M. M. Aziz, R. J. Hicken, Adv. Mater. **23**, 3408 (2011).

[31]G. M. Fischer, B. Medower, R. Revay, and M. Mansuripur, Appl. Opt. **41**, 1998 (2002).

[32]P. K. Khulbe, E. M. Wright, and M. Mansuripur, J. Appl. Phys. **88**, 3926 (2000).

[33]K. Kieu, K. Narumi and M. Mansuripur, Appl. Opt. **45**, 7826 (2006).

[34]K. Tajima, N. Kitamura, and N. T. Saiki, see http://jpcos.jp/Paper&Academic_etc/PCOS2011Papers/11%20Tajima_PCOS2011.pdf for Phase Change Oriented Science, Japan (2011).

[35]H. Huang, F. Zuo, F. Zhai, Y. Wang, T. Lai, Y. Wu, and F. Gan, J. Appl. Phys. **106**, 063501 (2009).

[36]H. Cheng, S. Raoux, and Y. Chen, J. Appl. Phys. **107**, 074308 (2010).

[37]M. Konishi, H. Santo, Y. Hongo, K. Tajima, M. Hosoi, and T. Saiki, Appl. Opt. **49**, 3470 (2010).

[38]J. Orava, A. L. Greer, B. Gholipour, D. W. Hewak, and C. E. Smith, Nature Mater. **11**, 279 (2012).